PAPER

Check for updates

In situ thermosensitive H₂O₂/NO self-sufficient hydrogel for photothermal ferroptosis of triple-negative breast cancer†

Sri Amruthaa Sankaranarayanan,[a] Kalyani Eswar,[a] Rupali Srivastava,[a] Ajinkya Madhukar Thanekar, [ID] [a] Mounika Gubige,[a] Veeresh Bantal[b] and Aravind Kumar Rengan [ID] *[a]

L-Arginine (LA), a semi-essential amino acid in the human body, holds significant potential in cancer therapy due to its ability to generate nitric oxide (NO) continuously in the presence of inducible NO synthase (iNOS) or reactive oxygen species (ROS). However, the efficiency of NO production in tumor tissue is severely constrained by the hypoxic and H₂O₂-deficient tumor microenvironment (TME). To address this issue, we have developed calcium peroxide (CaO₂) nanoparticles capable of supplying O₂/H₂O₂, which encapsulate and oxidize an LA-modified lipid bilayer to enable controlled localized NO generation in the presence of ROS, synergising with a ferroptosis inducer, RSL-3 (CPIR NPs). The synthesized nanoparticles were tested *in vitro* for their anticancer activity in 4T1 cells. To address challenges related to specificity and frequent dosing, we developed an *in situ* thermosensitive injectable hydrogel incorporating CPIR nanoparticles. Cross-linking at 60 °C creates a self-sufficient formulation, releasing NO/H₂O₂ to combat tumor hypoxia. RSL-3 induces ferroptosis, contributing to a synergistic photothermal effect and eliminating tumor *in vivo*.

Introduction

Nitric oxide (NO) is a critical molecule that regulates various physiological and biochemical processes. These include but are not limited to neuronal functioning and signalling, cardiovascular homeostasis, and, most importantly, immune response.[1,2] Recent evidence highlights that NO not only enhances the efficacy of existing therapeutic strategies, but also directly induces apoptosis in tumor cells at substantially high concentrations (>1 μM) through mitochondrial damage and DNA damage. These properties position NO as a potent therapeutic moiety for cancer therapies.[3–5] Although various NO sources, such as *S*-nitrosoglutathione, *S*-nitroso-*N*-acetyl penicillamine, and nitrate-functionalized D-α-tocopheryl polyethylene glycol succinate, have shown potential in NO-mediated tumor treatment, their clinical application is hindered by high costs; the physiological instability of these NO donors limits their bioavailability, leading to systemic toxici-

ties, subsequently limiting their feasibility in clinical scenarios.[6–8] L-Arginine (LA), a highly biocompatible and semi-essential amino acid in humans, serves as a natural precursor for NO formation when catalysed by inducible nitric oxide synthase (iNOS). Also, L-arg, upon reaction with reactive oxygen species (ROS, ₁O² and H₂O₂), can augment NO generation through a non-enzymatic pathway.[9–11] The tumor microenvironment is characterized by L-arg deficiency, leading to immune suppressive conditions. In addition, the hypoxic and H₂O₂-deficient TME hinders inherent NO formation.[12–15] Delivery of L-arg to the tumor site is limited by its short half-life and low bioavailability during circulation. Therefore, for leveraging the properties of L-arg, there is a strong demand to design novel nanocarriers for stable L-arg delivery and controlled NO release through self-supplementation of O₂ and H₂O₂.

Metal peroxide-based nanoparticles, often overlooked but significant in the realm of metal-involved nanosystems, serve as solid precursors for generating oxygen (O₂) and hydrogen peroxide (H₂O₂) through simple chemical reactions.[16–18] These metal peroxides, particularly calcium peroxide (CaO₂), exhibit promising potential in regenerative medicine and tumor treatment due to their good biocompatibility, high O₂ content, and prolonged O₂-releasing capacity. CaO₂, acting as "solid H₂O₂", reacts with water to rapidly generate H₂O₂, a reactive oxygen

ᵃDepartment of Biomedical Engineering, Indian Institute of Technology Hyderabad, Kandi, Sangareddy, Telangana 502284, India. E-mail: aravind@bme.iith.ac.in
ᵇG Pulla Reddy College of Pharmacy, Mehdipatinam, Hyderabad, India
†Electronic supplementary information (ESI) available. See DOI: https://doi.org/10.1039/d4nr02907k

species (ROS) with excellent antibacterial and antitumor effects.[19–26] The advent of Fenton reaction-based catalytic nanotherapeutics introduces a unique tumor-therapeutic modality with high specificity. This approach employs Fenton agents to convert tumor-overexpressed H_2O_2 into highly toxic hydroxyl radicals ($^{\cdot}OH$) for oxidative therapy.[27–30] However, the low intra-tumoral H_2O_2 levels substantially limit their therapeutic efficiency. Metal peroxides offer a solution by providing the potential for designing Fenton nanoagents for catalytic nanotherapeutics.

Ferroptosis, induced by iron-dependent accumulation of excessive lipid peroxides (LPOs), has gained attention in cancer therapy.[31–34] Ferroptosis, an iron-dependent mechanism, induces excessive ROS generation and lipid peroxidation, leading to cell lethality via Fenton's reaction. It is well reported that mitochondrial iron metabolism regulates ferroptotic cell death, leading to morphological changes and damage to membrane potential when cancer cells undergo ferroptosis. Additionally, excessive oxidative stress via ROS/lipid peroxides causes irreversible mitochondrial damage, leading to disrupted organelle integrity. Ferroptosis, as non-apoptotic programmed cell death, has been explored over the last decade in reversing the radioresistance and chemoresistance in several metastatic cancer cells through inhibition of the antioxidant pathways.

While photothermal therapy (PTT) relies on heat to inflict physical damage to cancer cells, the heightened expression of heat shock proteins (HSPs) triggered during PTT serves as a self-protective mechanism. This intrinsic defence mechanism not only diminishes the heat-induced damage but also hampers downstream biological responses. Recognizing this challenge, substantial efforts have been invested in integrating PTT with the inhibition of HSP expression, aiming to enhance therapeutic efficacy beyond the photothermal effect alone. Studies indicate that the upregulation of intracellular reactive oxygen species (ROS) and membrane lipid peroxidation (LPO) during the ferroptosis process can effectively inhibit the expression of HSPs. This inhibition, in turn, disrupts the self-protective response of cancer cells to heat. Furthermore, the Fenton reaction rate experiences a significant fourfold increase when the environmental temperature rises from 20 to 50 °C. This observation led us to hypothesize that a combined therapy approach involving PTT and ferroptosis could unlock substantial potential for synergizing their respective therapeutic effects to the maximum extent, thereby offering an enhanced strategy for cancer therapy.[35–40] Furthermore, the kinetics of H_2O_2/O_2 release significantly increase at higher temperatures, owing to the stimuli-responsive nature of CaO_2 nanoparticles. This allows integration with NIR photosensitizers for combined hypoxia relief and photothermal therapy.[41,42] In this study, we utilized O_2/H_2O_2-generating CaO_2 NPs for igniting NO generation upon photothermal trigger. The CaO_2 NPs were modified on its surface with L-arginine through liposomal coating. The nanosystem was integrated with IR806, a NIR sensitizer, and RSL-3 (CPIR NPs), a well-known and potent ferroptosis inducer. The initial focus of the article involves evaluating the anti-cancer efficacy of the CPIR NPs in 4T1 cells.

Despite advancements in the development of various nanosystems for targeted photothermal ferroptosis, the requirement of frequent dosing, short circulation time, and treatment of metastatic lesions remain a major challenge. Thermosensitive injectable hydrogels are gaining attention due to their various features like biocompatibility, biodegradability, stimuli sensitivity, sustained drug release, etc. Pluronic-based hydrogels are well reported to form micelles upon dissolution, featuring a polyethylene glycol chain on their surface that enhances steric stability and imparts stealth properties for prolonged circulation. The nano-transformation of the hydrogels, which can target and treat metastatic nodules irrespective of the site of primary injection, has been reported earlier.[43–49] In this study, we have modified a Pluronic-based thermosensitive hydrogel into a self-sufficient H_2O_2/NO injectable system to overcome the challenges of the hypoxic tumor microenvironment. This system enables the sustained release of drugs while promoting immune responses through the generation of nitric oxide (NO) and inducing immunogenic cell death via ferroptosis, specifically treating triple-negative breast cancer. (Scheme 1).

Results and discussion

Synthesis and characterization of L-arginine-modified CaO_2 liposomes

Bare calcium peroxide nanoparticles were prepared using a previously reported protocol with minor modifications. The size and morphology of the synthesized nanoparticles were characterized using SEM and TEM analyses. As shown in Fig. 1a and b, the nanoparticles were monodisperse with size ranging from 120 to 150 nm. The peroxide released from the CP NPs was evaluated using a colorimetric method, wherein $KMnO_4$ was mixed with the CaO_2 NPs dispersed in MQ water of pH 7.4 and 5.6, and H_2O_2 was used as a positive control and MQ water was used as a negative control. As shown in Fig. 1c, the $KMnO_4$ solution partially decolorized upon addition of the CaO_2 NPs at physiological pH 7.4 and completely degraded at acidic pH 5.6, comparable to that of H_2O_2, suggesting the reduction of MnO_4 to Mn^{2+} by the generated H_2O_2. This also
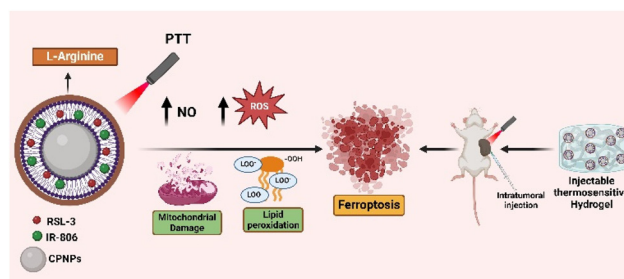
Scheme 1 Schematic illustrating the role of the CPIR NPs in inducing photothermal ferroptosis.
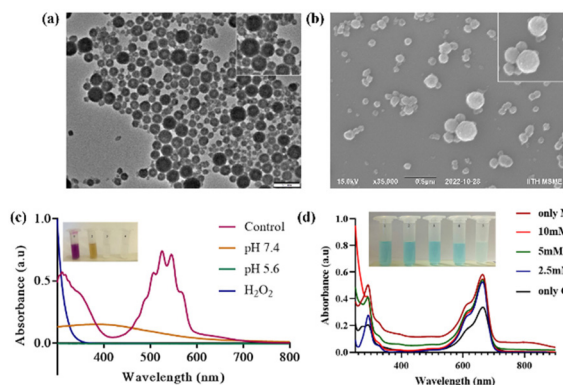
Fig. 1 Synthesis and characterization of the CP NPs. (a) TEM and (b) SEM images of the synthesized calcium peroxide nanoparticles. Evaluation of peroxide released from the synthesized nanoparticles using (c) the $KMnO_4$-based colorimetric method and (d) the methylene blue degradation method.

further indicates the pH-responsive nature of the CaO_2 NPs. To evaluate the ROS triggered by the CaO_2 NPs, methylene blue (MB) was selected as the indicator. Briefly, MB containing different concentrations of GSH, a potential ROS scavenger, was mixed with the CaO_2 NPs. As shown in Fig. 1d, with decreasing GSH concentration, there is an increase in MB degradation, as evident from the decolorization of the solution and the corresponding UV-Vis absorbance of MB. Even when the concentration of GSH was 10 mM, slight MB degradation was observed, due to the enhanced generation of ROS by the CaO_2 NPs (Fig. 1d).

To make the CaO_2 nanoparticles photothermally active, IR806 dye was loaded into the nanoparticles. As shown in ESI Fig. 1,† when the NIR dye was directly added to the synthesized CaO_2 NPs, due to the release of peroxide groups, there was an instant decolorization and degradation of the IR806 dye within 10 min. Hence, a previously reported strategy was adopted to load IR806 through modifying the CaO_2 NPs with liposomes on their surface. Briefly, a thin film containing HSPC : cholesterol : CaO_2 NPs : IR806 (10 : 1.8 : 1 : 1) was hydrated in 1 mM NH_5CO_3. The resulting nanoparticle solution was sonicated (20%-amp, 2 s pulse on and off) and centrifuged to remove the unbound reactants. L-Arginine (LA), a semi-essential amino acid present in the human body, has shown significant potential in cancer therapy. Its key attribute lies in its ability to continuously generate nitric oxide (NO) when exposed to inducible NO synthase (iNOS) or reactive oxygen species (ROS). Despite its promise, the efficiency of NO production in tumor tissue faces severe limitations within the hypoxic and H_2O_2-deficient tumor microenvironment (TME). Notably, the produced NO can exacerbate the abnormal retention of Ca^{2+} in the cells, leading to the amplification of oxidative stress and the induction of immunogenic cell death. Hence, IR806–CaO_2 liposomes were synthesized by modifying the hydration medium with L-arginine. The effect of L-arg incorporation was evaluated by comparing the nanoparticles

synthesized in other hydration media, *viz.*, MilliQ water, only L-arg, NH_5CO_3 and NH_5CO_3 + L-arg. The UV-Vis absorbance characteristics of the obtained nanoparticles were investigated (Fig. 2a). As seen in the inset bright light pictures, when the nanoparticles were synthesized in only MQ water, there was a complete degradation of the dye, whereas in the case of L-arg, there was a slight increase in the loading of IR806 dye. As discussed in the previous section, when hydration was performed using 1 mM NH_5CO_3, there was protection of the dye from degradation which significantly enhanced the encapsulation and this remained unaffected when further modified with L-arg. The obtained pellet was tested for the presence of L-arginine using the standard Sakaguchi test. As shown in Fig. 2b, the formation of red rings was evident in the case of control L-arg, nanoparticles synthesized in only L-arg and NH_5CO_3 + L-arg, proving the incorporation of L-arg. Furthermore, the photothermal temperature rise was evaluated upon NIR laser irradiation using an infrared thermal camera. As shown in Fig. 2c, compared to the control groups, for the same concentration of IR806, it is interesting to observe a substantial increase in the temperature in the case of NH_5CO_3 + L-arg. This could be attributed to the increased stability of IR806 in the presence of L-arg within the nanosystem, consistent with the previous reports. The corresponding thermal images are provided in ESI Fig. S2.†

To test the ignition of NO generation in the presence of ROS, 4T1 cells were treated with liposomes containing only IR806 modified with L-arginine (IA), liposomes containing IR806, and CaO_2 NPs (CI) and CI liposomes modified with L-arginine (CIA) and irradiated using a 750 nm NIR laser for 5 min. The amount of nitrite released in the supernatant was quantified using the Griess assay. As shown in Fig. 2d, in the presence of the CaO_2 NPs, due to enhanced ROS generation, the NO generated due to L-arg present in the nanoparticles was significantly higher than those of the respective control
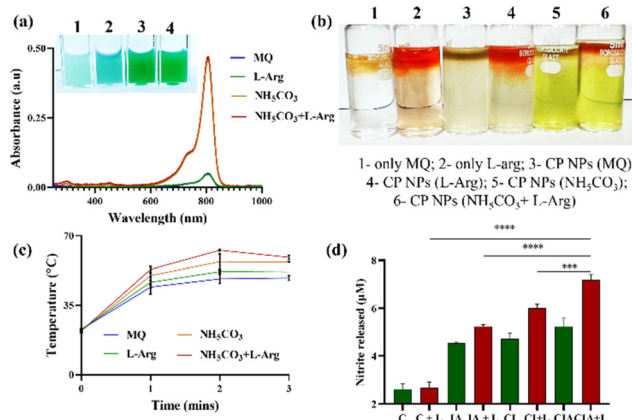
Fig. 2 Incorporation of L-arginine for NO release. (a) UV-Vis absorbance of the CPIR NPs synthesized in different hydration media, (b) confirmation of the presence of L-arg using the Sagakuchi test, (c) photothermal temperature rise upon NIR laser irradiation and (d) evaluation of NO release in 4T1 cells using the Griess assay.
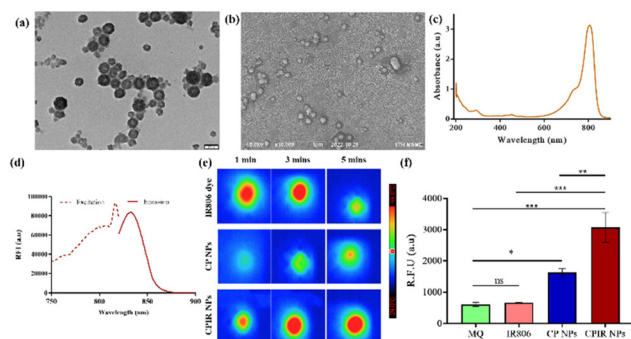
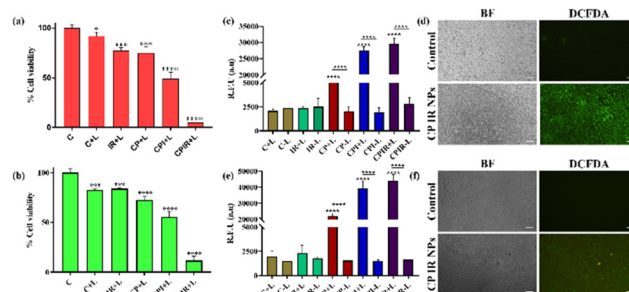groups. Hence, L-arginine modified NPs were used for further *in vitro* studies.

The CP NPs synthesized using NH_5CO_3 + L-arg were further loaded with a ferroptosis inducer, RSL-3 (CPIR NPs), and their size and morphology were characterized. As seen in the TEM image (Fig. 3a) and the SEM image (Fig. 3b), a coating surrounding the nanoparticles was visible, confirming the modified liposome on the surface. The UV-Vis absorbance, fluorescence and photothermal transduction properties of the resulting CPIR NPs were investigated. The standard curve for RSL-3 is provided in ESI Fig. 3.† As shown in Fig. 3c, the characteristic peak of IR806 was observed at 806 nm and that of RSL-3 was observed at 203 nm and the corresponding fluorescence (Fig. 3d) was recorded. The photothermal temperature rise of free IR806 was compared with that of IR806 loaded into the CaO_2 NPs and, as shown in Fig. 3e, the encapsulation of the dye within a nanosystem significantly improved its photothermal stability, compared to the free dye, which is prone to photo-degradation. As shown in Fig. 3f, there was a significant increase in ROS generation in the case of the CPIR NPs upon laser irradiation.

Evaluation of NIR laser-mediated cytotoxicity and ROS generation

For a synergistic photothermal ferroptosis, RSL-3, a class 2 ferroptotic inducer, was used upon co-encapsulation with IR806-loaded CaO_2 liposomes (CPIR NPs). The laser-mediated cytotoxicities of these nanoparticles were tested in 4T1 cells maintained under normal and hypoxic conditions (IR – IR806-loaded liposomes, CP – CaO_2 NP-loaded liposomes, CPI – IR806-loaded CaO_2 NP liposomes and CPIR – RSL-3- and IR806-loaded CaO_2 liposomes). As shown in Fig. 4a and b, CPIR exhibited significant cytotoxicity under both normoxic and hypoxic conditions, compared to the respective controls. The CaO_2-mediated ROS generation was evaluated in the cells using the DCFDA assay. As shown in Fig. 4c–f, the ROS generated in the CPI- and CPIR NP-treated groups were significantly
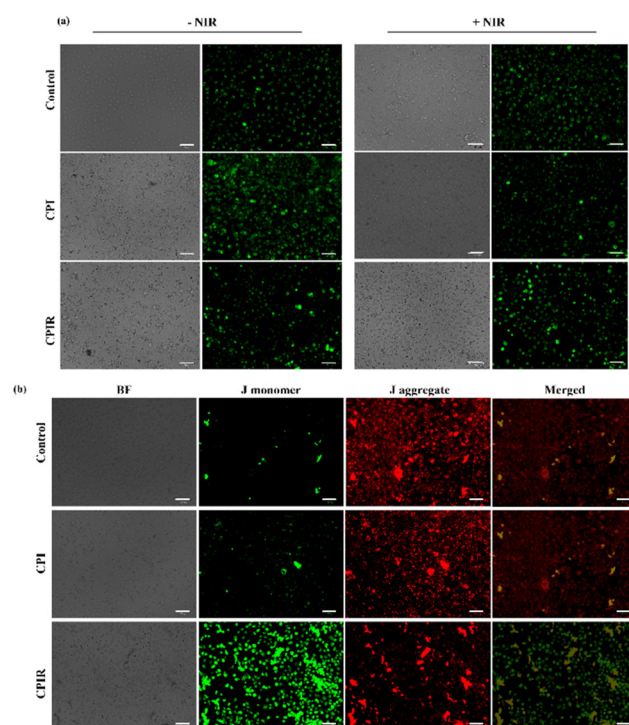

Fig. 4 Evaluation of NIR-mediated cytotoxicity. PTT-mediated cytotoxicity of the CPIR NPs under (a) normoxic and (b) hypoxic conditions. Qualitative assessment of ROS-generated and the corresponding fluorescence images using the DCFDA assay in 4T1 cells maintained under (c and d) normoxic conditions and (e and f) hypoxic conditions (scale bar represents 100 μm).

higher upon NIR laser irradiation, due to the heat generated by the presence of IR806, a characteristic feature of the CaO_2 NPs).

Evaluation of mitochondrial damage

Ferroptosis is associated with the dysregulation of mitochondrial functions, such as regulation of Ca^{2+}, damage of membrane potential, *etc*. The mitochondrial morphology was evaluated by staining with MitoTracker Green. As shown in Fig. 5a, in the CPIR-treated cells upon NIR laser irradiation, there was

Fig. 3 Synthesis and characterization of the CPIR NPs. (a) TEM – direct loading of IR806 dye into the calcium peroxide nanoparticles, (b) SEM – encapsulation of IR806 into the CP NPs through NH_5CO_3–modified liposome coating, (c) UV-Vis absorbance spectra, (d) fluorescence spectra and (e) photothermal temperature upon NIR laser irradiation of the CPI NPs and (f) ROS generation in the CPIR NPs upon laser irradiation.

Fig. 5 Evaluation of PTT-mediated mitochondrial damage. PTT-mediated effect on mitochondria using (a) MitoTracker Green staining and (b) JC1 staining (scale bar represents 58 μm).

an evident loss of morphology as compared to the control groups. Hence, JC1 staining was further performed on laser irradiated CPI- and CPIR-treated cells. As shown in Fig. 5b, there was a significant increase in the green fluorescence in the CPIR-treated cells, showing that the dysregulated mitochondrial membrane potential is due to photothermal ferroptosis.

Evaluation of the anti-migration effect

Cancer cell migration is a major hallmark for invasion and metastasis. Hence, the migration abilities of the cells treated with CPI and CPIR upon laser irradiation were evaluated through a scratch assay. As shown in Fig. 6, due to the presence of RSL-3, the cells lost their morphology and ability to migrate to close the created wound. The viability of the cells in the wounded area was assessed using FDA/PI staining, showing that the loss of morphology in the CPIR-treated groups is due to cell death.

CAM assay

CAM assay was performed to assess the PTT-mediated rupturing of blood vessels, a process that could inhibit angiogenesis and nutrient supply around the tumor region. As shown in Fig. 7, significant blood vessel rupturing was found in the CPIR-treated group upon NIR laser irradiation due to the photothermal effect of IR806 present in the CaO_2 liposomes.

From the above *in vitro* studies, it was evident that the RSL-3 combined with L-arginine modification of IR806-loaded CaO_2 liposomes results in enhanced photothermal ferroptosis due to RSL-3 and ignited NO generation in the presence of ROS produced by CaO_2 from the heat generated by IR806 present in the NPs.

Preparation and characterization of the *in situ* thermosensitive hydrogel (CPR-NTG)

The anti-cancer efficacy of the IR806-loaded CaO_2 liposomes loaded with RSL-3 was tested in 4T1 cells. However, for an efficient therapeutic efficacy, it requires multiple and frequent dosings of these nanosystems. Also, a localized trigger-induced
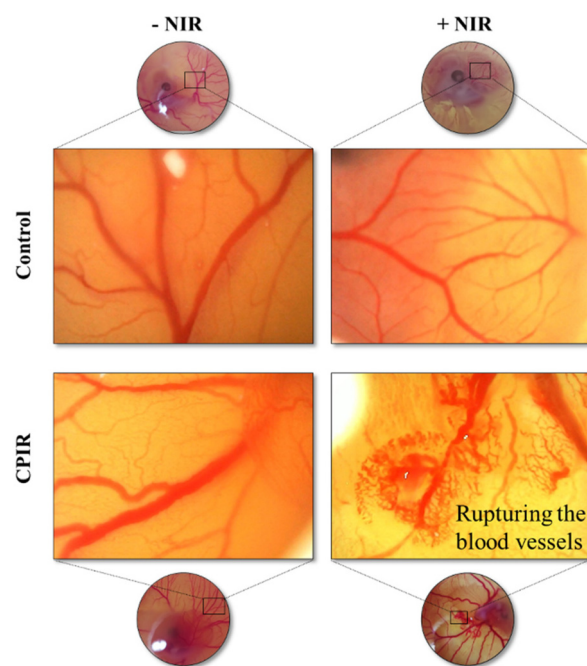

Fig. 7 Evaluation of PTT-mediated blood vessel rupturing using a CAM assay model.

therapeutic could protect the surrounding normal tissues from its toxic side effects. Hence, to overcome such challenges, an injectable and *in situ* nano-transformable hydrogel was developed, which upon cross linking at 60 °C degrades into self-stabilized nanoparticles capable of targeting secondary tumor sites *via* the EPR effect. The as-developed CPIR NPs were loaded within the hydrogel, and when cross-linked using the NIR trigger, the hydrogel could be tuned into a self-H_2O_2/NO sufficient formulation to combat the hypoxic conditions of the tumor core and ignite the NO production in the presence of ROS generated. Also, the presence of RSL-3 within the formulation aids in a synergistic photothermal effect by inducing ferroptosis, which in turn can evoke an inherent immune response that could aid in an abscopal effect.

The gelling properties of the synthesized hydrogel were evaluated using the tube-inversion method, upon crosslinking at 37 °C and 60 °C, as shown in Fig. 8a. The peroxide released from the hydrogel upon cross-linking at 60 °C was evaluated using the $KMnO_4$-based colorimetric method. As shown in Fig. 8b, the $KMnO_4$ solution decolorized when added to CaO_2 NTG.

The cross-linking of the hydrogel at 37 °C and 60 °C was confirmed using SEM analysis. As shown in Fig. 8c, albumin-mediated crosslinking at 60 °C was evident with obvious cross-linking patterns, whereas no such cross-linking was observed in the sample crosslinked at 37 °C. This temperature could be achieved using NIR irradiation in *in vivo* studies due to the presence of IR806 within the hydrogel.

Rheological studies were performed on the bare and CP NP-based NTGs to assess the impact of calcium peroxide on the
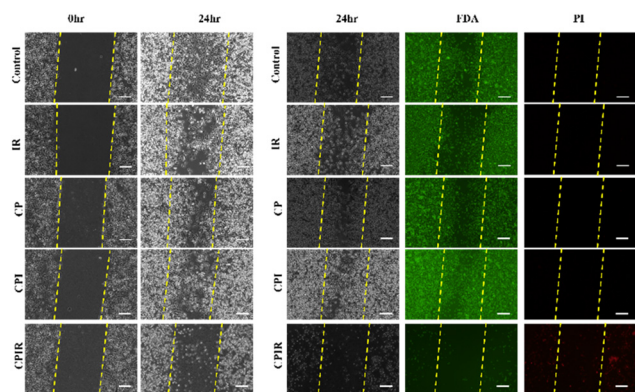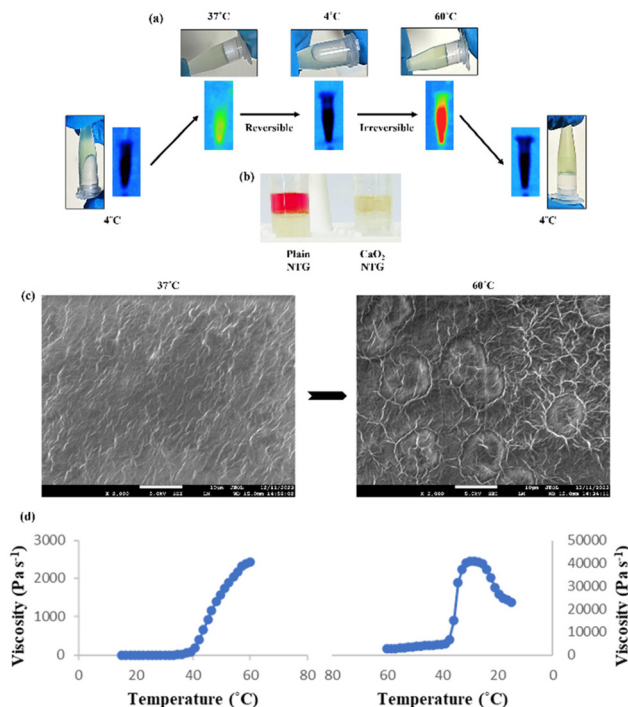

Fig. 6 Evaluation of the PTT-mediated anti-migration effect on 4T1 cells treated with the CPIR NPs (scale bar represents 100 μm).
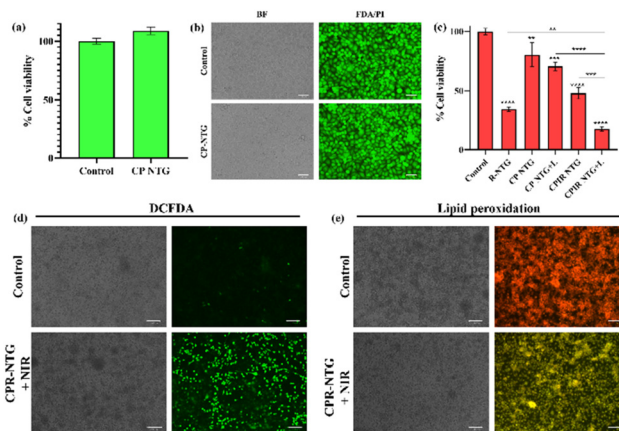
Fig. 8 Characterization of CPR NTG. (a) Tube-inversion test showing the reversible and irreversible cross-linking of hydrogel formation, (b) evaluation of peroxide release using the potassium permanganate colorimetric method, (c) SEM analysis of the hydrogel crosslinked at 37 °C and 60 °C and (d) rheological analysis of CPR NTG.

Fig. 9 *In vitro* studies using CPR NTG. (a) Biocompatibility of the developed CP NTG and (b) the corresponding live/dead imaging in L929 cells. (c) Cytotoxicity of the developed CPIR NTG, (d) ROS generation using the DCFDA assay and (e) evaluation of lipid peroxidation in 4T1 cells (scale bar represents 50 μm in (b) and 100 μm in (d) and (e)).

hydrogel's viscosity. Both bare NTG and CPIR NTG showed minimal viscosity at 4 °C and underwent phase transitions at around 25 °C, which is crucial for injectability. The changes observed in the viscosity upon exposure to elevated temperature further indicate the cross-linking of the hydrogel. Additionally, the irreversible cross-linking of the gel at 60 °C was further confirmed using the reverse thermal sweep test. It was evident that the presence of calcium peroxide NPs did not alter the rheological properties of the hydrogel, supported by FTIR analysis (Fig. 8d and ESI Fig. S5, S6†).

Furthermore, the photothermal temperature rise was recorded by irradiating the nanoparticles in solution and the hydrogel using an 808 nm laser. As shown in ESI Fig. S7a,† in the case of the nanoparticle solution, the temperature rise was recorded to be 50 °C, whereas in the case of the hydrogel, the temperature rise was recorded to be 77 °C. It is evident that incorporation of the nanoparticles into the hydrogel could potentially enhance the stability and inhibit the photo-degradation of the NIR dye. The photothermal stability of the samples was also evaluated for three cycles of repeated heating and cooling. As shown in ESI Fig. S7b,† when incorporated into the hydrogel, the photothermal stability was much higher compared to the solution form, which could be advantageous for a localized therapy using the developed hydrogel.

Furthermore, the biocompatibility of the developed hydrogel was evaluated in L929 cells. For this, only the CPI NP

(calcium peroxide encapsulated with IR806)-loaded hydrogel was used without RSL-3. As shown in Fig. 9a, the CPI NP-loaded hydrogel (CP NTG) did not exert any cytotoxicity in L929 cells compared to the control group, and was also qualitatively assessed using live/dead staining (Fig. 9b). Additionally, the cytotoxicity of the hydrogel was evaluated in 4T1 cells using various formulations: RSL-3-loaded hydrogel (R-NTG), CP NTG (crosslinked at 37 °C), CP NTG + L (crosslinked at 60 °C with NIR irradiation), CPIR NTG (crosslinked at 37 °C), and CPIR NTG + L (crosslinked at 60 °C with NIR irradiation). As shown in Fig. 9c, the presence of RSL-3 significantly reduced the cell viability, when loaded alone and in combination with the CPIR NPs, with a significant increase in the case of CPIR NTG upon laser irradiation, which could be due to the increase in the rate of ferroptosis from the ROS/NO generated upon laser irradiation. The ROS generated upon treatment with CPIR NTG + L was qualitatively assessed using the DCFDA assay. As shown in Fig. 9d, there was a significant increase in the green fluorescence in the case of CPIR NTG + L compared to the other groups (ESI Fig. S8†). Lipid peroxidation, a major hallmark of ferroptosis cell death, was assessed using a lipid peroxidation sensor, with which the inherent red fluorescence shifts to green in the presence of lipid peroxides. As shown in Fig. 9e, in the case of CPIR NTG + L, there was a substantial increase in the green fluorescence compared to the control groups (ESI Fig. S9†), indicating the synergistic CPIR NTG-mediated photothermal ferroptosis.

In vivo studies

All animal procedures were performed in accordance with the Guidelines for Care and Use of Laboratory Animals and approved by the Animal Ethics Committee of G Pulla Reddy College of Pharmacy, Hyderabad, India (GPRCP/IAEC-1/24/08/2022/PCL/AE-6). Prior to testing the anti-cancer efficacy of the CPIR NPs and CPIR NTG, their *in vivo* photothermal transduc-

tion efficacy was initially evaluated. The animals injected with only the CPIR NPs exhibited a temperature rise of up to just 45 °C upon 3 min of laser irradiation, which further declined after 3 cycles of laser irradiation. However, in CPIR-NTG, a sustained photothermal effect was observed with the temperature rising up to >60 °C and a stable increase in the temperature up to 3 cycles of laser irradiation (Fig. 10a–c). As shown in Fig. 10d, in the case of s.c.-injected CPIR NPs, the nanoparticles had degraded from the localized site post-three cycles of irradiation, whereas in the case of s.c.-injected CPIR NTG, the hydrogel was still localized in the injected area (marked in yellow). These findings confirm the sustained *in vivo* photothermal transduction of CPIR NTG at the site of injection, thereby reducing the need for multiple dosages.

A 4T1 cell-induced syngeneic breast cancer model was used to study the intratumoral temperature rise and photothermal efficacy in balb/c mice. 4T1 tumor cells (1×10^6) were implanted subcutaneously near the breast fat of a mammary gland. The mice were randomly divided into four groups ($n = 3$) and treated intratumorally with R-NTG, CPI-NTG and CPIR-NTG. The tumor region was irradiated with NIR light for three cycles (2 min ON; 2 min OFF). The anti-cancer efficacy was further evaluated upon irradiating the tumor bearing mice with an 808 nm, 650 mW NIR laser for 3 min. The tumor volume and body weight were monitored at definite time intervals (ESI Fig. S10†). No abnormal behaviours were observed

during the course of the treatment period. As shown in Fig. 10e and f, the CPIR-NTG group showed significant tumor inhibition, with the disappearance of tumor a week post-irradiation, although an obvious scar was found on the mice, while the tumor volumes of the R-NTG-treated group showed a slight decrease when compared with the control groups. This study shows the role of the developed hydrogel in inducing synergistic photothermal ferroptosis at the primary tumor site. Splenomegaly (spleen enlargement) is positively correlated with the extent of cancer burden as a result of a leukemoid-like reaction when 4T1 cells are implanted in BALB/c mice. Interestingly, groups treated with the developed hydrogel showed a significant reversal of splenomegaly, exhibiting a remarkable systemic response in addition to suppressing the localized tumor (Fig. 10g and h). ESI Fig. S11† shows the triplicate photographs of excised tumors and the spleen.

Histopathological analysis revealed necrotic cell damage and inflammatory lesions in tumors treated with CPR NTG, with milder effects observed in R-NTG-treated tumors. The spleen microarchitecture remained relatively normal in the mice treated with CPR-NTG, resembling that of healthy controls, highlighting the therapeutic potential of the developed nanosystem (ESI Fig. S12 and S13†).

Materials and methods

Synthesis and characterization of L-arginine-modified CaO₂ liposomes

CP NPs were synthesized using previously reported methods with slight modifications. Briefly, calcium hydroxide and PVP were dissolved in a 1 : 6 ratio in 15 mL of MilliQ water. Under stirring, 500 μL of H_2O_2 was added drop by drop and allowed to react for 10 min. The solution was then centrifuged at 10 000 rpm for 10 minutes. The pellet was washed thrice with ethanol and allowed to air dry overnight to obtain a powdered pellet. The size and morphology of the synthesized CaO_2 NPs were characterized using Scanning Electron Microscopy (SEM, JEOL, Japan) and Transmission Electron Microscopy (TEM, JEOL JEM F200, Japan).

IR806-loaded CaO_2 liposomes were prepared using a previously reported strategy. Briefly, HSPC, cholesterol, CaO_2 and IR806 were dissolved in a ratio of 10 : 1.8 : 1 : 1 in a 2 : 1 chloroform : methanol mixture and subjected to thin film formation in a rotavapor at 45 °C for 45 min. The formed thin film was hydrated in 1 mM NH_5CO_3 containing 100 mg of L-arginine. The synthesized nanoparticles were sonicated (20% amplitude with 2 s on and off) and centrifuged at 15 000 rpm for 15 min. The obtained pellet was resuspended in 1 mL of MilliQ water. The presence of L-arginine in the nanoparticles was tested using the Sakaguchi test.

In vitro studies

Evaluation of NO release in 4T1 cells. Briefly, seeded 4T1 cells were treated with liposomes containing only IR806 modified with L-arginine (IA), liposomes containing
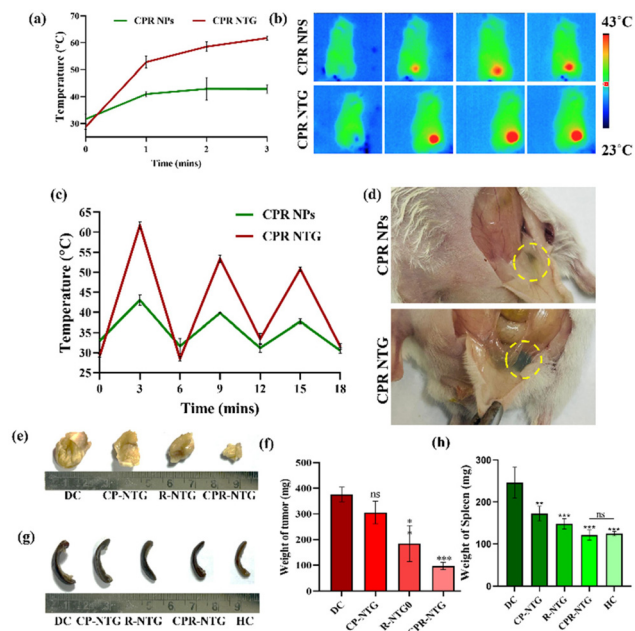
Fig. 10 *In vivo* studies using CPIR NTG. (a) Photothermal temperature rise of the s.c.-injected CPIR NPs and CPIR-NTG and (b) the corresponding thermal images upon NIR laser irradiation. (c) Photothermal stability of the s.c.-injected CPIR NPs and CPIR-NTG after 3 cycles of NIR laser irradiation. (d) Photographs of mice s.c.-injected with CPIR NPs and CPIR NTG after 3 cycles of NIR laser irradiation. (e) Photographs and (f) weights of the excised tumors. (g) Photographs and (h) weights of the excised spleen.

IR806 and the CaO$_2$ NPs (CI) and CI liposomes modified with L-arginine (CIA) and irradiated with a 750 nm laser for 5 min. Post-24 h of irradiation, the supernatant of the treated cells was collected and the NO released was quantified using the Griess assay.

Evaluation of NIR laser-mediated cytotoxicity and ROS generation. Briefly, seeded 4T1 cells were treated with IR – IR806-loaded liposomes, CP – CaO$_2$ NP-loaded liposomes, CPI – IR806-loaded CaO$_2$ NP liposomes and CPIR – RSL-3- and IR806-loaded CaO$_2$ liposomes. The cells were then irradiated using a 750 nm laser for 5 min. 24 h post-irradiation, the viability of the cells was quantified using the MTT assay. The cells were maintained under hypoxic conditions by treating with 40 µg mL^{-1} cobalt chloride for 12 hours prior to treatment and the MTT assay was performed with the similar procedures mentioned above.

The DCFDA assay was performed to assess the ROS generated upon NIR laser irradiation. Briefly, the cells were treated with IR, CPI and CPIR, and 1 µl of 10 mM DCFDA was added. The cells were then irradiated using a 750 nm NIR laser and the fluorescence intensity was recorded using a spectrofluorometer (Ex: 485 nm & Em: 535 nm). The ROS generated in the cells were further captured under a fluorescence microscope.

Evaluation of mitochondrial damage. The morphology of mitochondria upon treatment with IR, CPI and CPIR and NIR laser irradiation were qualitatively assessed by staining the mitochondria using MitoTracker Green. Briefly, 12 hours post-irradiation, the cells were washed and 5 mM MitoTracker Green was added. Then they were incubated for 30 min. The cells were further washed with 1× PBS and imaged under a live cell imager (Zoe, Bio-Rad, USA). For JC1 staining, 12 hours post-irradiation, 10 µg mL^{-1} JC-1 dye was added to the NIR-irradiated cells and incubated for 20 min. The cells were then washed with 1× PBS and imaged under a live cell imager (Zoe, Bio-Rad, USA).

Evaluation of the anti-migration effect. Briefly, 4T1 cells seeded in a 24-well plate were treated with IR, CPI and CPIR and irradiated with a 750 nm NIR laser for 5 min. 6 hours post-irradiation, a scratch was introduced using a 200 µL tip and imaged at 0th and 24th hours to evaluate the migration of the cells. The viability of the cells in the wounded area was qualitatively assessed using FDA/PI-based live/dead staining at the 24th hour.

Preparation and characterization of the *in situ* thermosensitive hydrogel (CPR-NTG). Briefly, to prepare a thermosensitive hydrogel, 0.6 mL of PVA solution was added slowly drop-by-drop to 3 mL of Pluronic F-127 (25% w/v) at 4 °C under constant stirring and furthermore, 500 µL of bovine albumin (35% w/v, ice-cold) was added dropwise under continuous stirring.[43] For the preparation of the NIR-responsive H$_2$O$_2$/NO self-sufficient hydrogel, the hydrogel was mixed with the CPIR NPs, keeping the concentration of IR806 at 50 µg mL^{-1}. The thermosensitive nature of the developed hydrogel was further characterized using the tube-inversion method. The crosslinking was further analysed by characterizing the rheological parameters (viscosity *vs.* temperature) and SEM analysis. The photothermal temperature rise was recorded by irradiating the same concentration of NPs in solution and in the hydrogel using an 808 nm laser for 3 min. The rise in temperature was recorded using an infrared thermal camera. Furthermore, the photothermal stability was also evaluated for three cycles.

In vivo studies

We preliminarily assessed the anti-cancer efficacy of the developed hydrogel in a 4T1-induced breast cancer model in Balb/c mice. All animal procedures were performed in accordance with the Guidelines for Care and Use of Laboratory Animals and approved by the Animal Ethics Committee of G Pulla Reddy College of Pharmacy, Hyderabad, India (GPRCP/IAEC-1/24/08/2022/PCL/AE-6). Briefly, post-1 week of the acclimatization period, 1×10^6 4T1 cells were subcutaneously injected to the fat pad of the mammary gland. Once a palpable tumor size was achieved, the mice were randomly divided into 4 groups (disease control, CP NTG (gel containing only IR-loaded calcium peroxide nanoparticles), R NTG (gel containing only RSL-3) and CPIR NTG (gel containing CPIR NPs)). The nanoparticles were intratumorally injected, and the tumor region was irradiated with an 808 nm laser for 3 min. The tumor volume and body weight were recorded at definite time intervals. After the treatment period, the animals were euthanized, and the organs were excised.

Statistical analysis

All the statistical analyses were performed using one-way ANOVA (ns: $P > 0.05$, * $P < 0.05$, ** $P < 0.01$, *** $P < 0.001$, and **** $P < 0.0001$). Throughout the manuscript, the error bars indicate the standard deviation in the mean.

Conclusions

The presence of L-arginine in CaO$_2$ liposomes was found to ignite NO generation in 4T1 cells upon NIR laser irradiation. The combination of L-arg-modified CaO$_2$ with RSL-3, a potent ferroptosis inducer, was found to exert significant cytotoxicity in 4T1 cells maintained under normoxic and hypoxic conditions through enhanced ROS generation and mitochondrial damage. The PTT efficacy was also found to cause significant blood-vessel rupturing in a CAM model. A thermosensitive hydrogel self-sufficient in H$_2$O$_2$/NO was developed by encapsulating the above tested CPIR NPs. The irreversible crosslinking of the developed hydrogel at 60 °C through NIR trigger was characterized using SEM imaging and rheological characterization.

Author contributions

Sri Amruthaa Sankaranarayanan: conceptualization, data curation, methodology, software, validation, writing – original draft, review and editing; Kalyani Eswar: data curation, validation, writing – original draft, review and editing; Rupali

Srivastava: data curation and validation; Ajinkiya Mathukar Thanekar: data curation; Mounika Gubige: data curation; Veeresh Bantal: supervision, methodology and validation; Aravind Kumar Rengan: conceptualization, supervision, funding acquisition, project administration, validation, writing – original draft, review and editing.

Data availability

The data supporting this article have been included as part of the ESI† and are a part of an ongoing study.

Conflicts of interest

There are no conflicts to declare.

Acknowledgements

References

1 J. W. Coleman, Nitric oxide in immunity and inflammation, *Int. Immunopharmacol.*, 2001, **1**(8), 1397–1406.

2 H. Y. Yun, V. L. Dawson and T. M. Dawson, Neurobiology of nitric oxide, *Crit. Rev. Neurobiol.*, 1996, **10**, 291–316.

3 D. Fukumura, S. Kashiwagi and R. K. Jain, The role of nitric oxide in tumour progression, *Nat. Rev. Cancer*, 2006, **6**(7), 521–534.

4 Y. C. Sung, P. R. Jin, L. A. Chu, F. F. Hsu, M. R. Wang, C. C. Chang, S. J. Chiou, J. T. Qiu, D. Y. Gao, C. C. Lin and Y. S. Chen, Delivery of nitric oxide with a nanocarrier promotes tumour vessel normalization and potentiates anticancer therapies, *Nat. Nanotechnol.*, 2019, **14**(12), 1160–1169.

5 M. M. Wan, H. Chen, Z. Da Wang, Z. Y. Liu, Y. Q. Yu, L. Li, Z. Y. Miao, X. W. Wang, Q. Wang, C. Mao and J. Shen, Nitric oxide–driven nanomotor for deep tissue penetration and multidrug resistance reversal in cancer therapy, *Adv. Sci.*, 2021, **8**(3), 2002525.

6 W. Fan, B. C. Yung and X. Chen, Stimuli–responsive NO release for on–demand gas–sensitized synergistic cancer therapy, *Angew. Chem., Int. Ed.*, 2018, **57**(28), 8383–8394.

7 E. Y. Zhou, H. J. Knox, C. J. Reinhardt, G. Partipilo, M. J. Nilges and J. Chan, Near-infrared photoactivatable nitric oxide donors with integrated photoacoustic monitoring, *J. Am. Chem. Soc.*, 2018, **140**(37), 11686–11697.

8 J. F. Quinn, M. R. Whittaker and T. P. Davis, Delivering nitric oxide with nanoparticles, *J. Controlled Release*, 2015, **205**, 190–205.

9 M. Zhang, H. Jin, Y. Liu, L. Wan, S. Liu and H. Zhang, L-Arginine self-delivery supramolecular nanodrug for NO gas therapy, *Acta Biomater.*, 2023, **169**, 517–529.

10 S. H. Kim, J. Roszik, E. A. Grimm and S. Ekmekcioglu, Impact of l-arginine metabolism on immune response and anticancer immunotherapy, *Front. Oncol.*, 2018, **8**, 67.

11 L. B. Vong and Y. Nagasaki, Nitric oxide nano-delivery systems for cancer therapeutics: Advances and challenges, *Antioxidants*, 2020, **9**(9), 791.

12 S. Kudo and Y. Nagasaki, Novel nitric oxide-based anti-cancer therapeutics by macrophage-targeted poly (l-arginine)-based nanoparticles, *J. Controlled Release*, 2015, **217**, 256–262.

13 M. Wang, Z. Hou, S. Liu, S. Liang, B. Ding, Y. Zhao, M. Chang, G. Han, A. A. Kheraif and J. Lin, A multifunctional nanovaccine based on L–arginine–loaded black mesoporous titania: ultrasound–triggered synergistic cancer sonodynamic therapy/gas therapy/immunotherapy with remarkably enhanced efficacy, *Small*, 2021, **17**(6), 2005728.

14 R. M. Palmer, D. S. Ashton and S. Moncada, Vascular endothelial cells synthesize nitric oxide from L-arginine, *Nature*, 1988, **333**(6174), 664–666.

15 H. Hao, M. Yu, Y. Yi, S. Sun, X. Huang, C. Huang, Y. Liu, W. Huang, J. Wang, J. Zhao and M. Wu, Mesoporous calcium peroxide-ignited NO generation for amplifying photothermal immunotherapy of breast cancer, *Chem. Eng. J.*, 2022, **437**, 135371.

16 H. Hu, L. Yu, X. Qian, Y. Chen, B. Chen and Y. Li, Chemoreactive nanotherapeutics by metal peroxide-based nanomedicine, *Adv. Sci.*, 2021, **8**(1), 2000494.

17 S. N. Mbugua, Targeting tumor microenvironment by metal peroxide nanoparticles in cancer therapy, *Bioinorg. Chem. Appl.*, 2022, **2022**(1), 5041399.

18 J. He, L. H. Fu, C. Qi, J. Lin and P. Huang, Metal peroxides for cancer treatment, *Bioactive materials*, 2021, **6**(9), 2698–2710.

19 C. C. Huang, W. T. Chia, M. F. Chung, K. J. Lin, C. W. Hsiao, C. Jin, W. H. Lim, C. C. Chen and H. W. Sung, An implantable depot that can generate oxygen in situ for overcoming hypoxia-induced resistance to anticancer drugs in chemotherapy, *J. Am. Chem. Soc.*, 2016, **138**(16), 5222–5225.

20 C. W. Chang and M. J. Wang, Preparation of microfibrillated cellulose composites for sustained release of H₂O₂ or

O2 for biomedical applications, *ACS Sustainable Chem. Eng.*, 2013, **1**(9), 1129–1134.

21 M. Zhang, R. Song, Y. Liu, Z. Yi, X. Meng, J. Zhang, Z. Tang, Z. Yao, Y. Liu, X. Liu and W. Bu, Calcium-overload-mediated tumor therapy by calcium peroxide nanoparticles, *Chem*, 2019, **5**(8), 2171–2182.

22 X. Wu, X. Han, Y. Guo, Q. Liu, R. Sun, Z. Wen and C. Dai, Application prospect of calcium peroxide nanoparticles in biomedical field, *Reviews on Advanced Materials Science*, 2023, **62**(1), 20220308.

23 Y. Hu, X. Wang, P. Zhao, H. Wang, W. Gu and L. Ye, Nanozyme-catalyzed oxygen release from calcium peroxide nanoparticles for accelerated hypoxia relief and image-guided super-efficient photodynamic therapy, *Biomater. Sci.*, 2020, **8**(10), 2931–2938.

24 S. Liu, H. Lai, F. Xing and P. Xiao, Polymer-coated calcium peroxide nanoparticles as an oxygen self-supplying platform for enhanced photodynamic therapy, *Eur. Polym. J.*, 2022, **177**, 111458.

25 C. He, X. Zhang, C. Chen, X. Liu, Y. Chen, R. Yan, T. Fan, Y. Gai, R. J. Lee, X. Ma and J. Luo, A solid lipid coated calcium peroxide nanocarrier enables combined cancer chemo/chemodynamic therapy with O_2/H_2O_2 self-sufficiency, *Acta Biomater.*, 2021, **122**, 354–364.

26 H. Hao, M. Yu, Y. Yi, S. Sun, X. Huang, C. Huang, Y. Liu, W. Huang, J. Wang, J. Zhao and M. Wu, Mesoporous calcium peroxide-ignited NO generation for amplifying photothermal immunotherapy of breast cancer, *Chem. Eng. J.*, 2022, **437**, 135371.

27 Y. Wang, F. Gao, X. Li, G. Niu, Y. Yang, H. Li and Y. Jiang, Tumor microenvironment-responsive fenton nanocatalysts for intensified anticancer treatment, *J. Nanobiotechnol.*, 2022, **20**(1), 69.

28 X. Qian, J. Zhang, Z. Gu and Y. Chen, Nanocatalysts-augmented Fenton chemical reaction for nanocatalytic tumor therapy, *Biomaterials*, 2019, **211**, 1–3.

29 Y. Han, S. Gao, Y. Zhang, Q. Ni, Z. Li, X. J. Liang and J. Zhang, Metal-based nanocatalyst for combined cancer therapeutics, *Bioconjugate Chem.*, 2020, **31**(5), 1247–1258.

30 X. Meng, X. Zhang, M. Liu, B. Cai, N. He and Z. Wang, Fenton reaction-based nanomedicine in cancer chemodynamic and synergistic therapy, *Appl. Mater. Today*, 2020, **21**, 100864.

31 L. H. Fu, C. Qi, Y. R. Hu, J. Lin and P. Huang, Glucose oxidase–instructed multimodal synergistic cancer therapy, *Adv. Mater.*, 2019, **31**(21), 1808325.

32 R. Liang, Y. Li, M. Huo, H. Lin and Y. Chen, Triggering sequential catalytic fenton reaction on 2D MXenes for hyperthermia-augmented synergistic nanocatalytic cancer therapy, *ACS Appl. Mater. Interfaces*, 2019, **11**(46), 42917–42931.

33 R. Liang, Y. Chen, M. Huo, J. Zhang and Y. Li, Sequential catalytic nanomedicine augments synergistic chemodrug and chemodynamic cancer therapy, *Nanoscale Horiz.*, 2019, **4**(4), 890–901.

34 M. Huo, L. Wang, Y. Chen and J. Shi, Tumor-selective catalytic nanomedicine by nanocatalyst delivery, *Nat. Commun.*, 2017, **8**(1), 357.

35 Y. Liu, P. Bhattarai, Z. Dai and X. Chen, Photothermal therapy and photoacoustic imaging via nanotheranostics in fighting cancer, *Chem. Soc. Rev.*, 2019, **48**(7), 2053–2108.

36 Y. Jiang, X. Zhao, J. Huang, J. Li, P. K. Upputuri, H. Sun, X. Han, M. Pramanik, Y. Miao, H. Duan and K. Pu, Transformable hybrid semiconducting polymer nanozyme for second near-infrared photothermal ferrotherapy, *Nat. Commun.*, 2020, **11**(1), 1857.

37 S. P. Sun, C. J. Li, J. H. Sun, S. H. Shi, M. H. Fan and Q. Zhou, Decolorization of an azo dye Orange G in aqueous solution by Fenton oxidation process: Effect of system parameters and kinetic study, *J. Hazard. Mater.*, 2009, **161**(2–3), 1052–1057.

38 F. Zeng, L. Tang, Q. Zhang, C. Shi, Z. Huang, S. Nijiati, X. Chen and Z. Zhou, Coordinating the mechanisms of action of ferroptosis and the photothermal effect for cancer theranostics, *Angew. Chem.*, 2022, **134**(13), e202112925.

39 H. Yu, J. Yan, Z. Li, T. Song, F. Ning, J. Tan and Y. Sun, Enhanced photothermal-ferroptosis effects based on RBCm-coated PDA nanoparticles for effective cancer therapy, *J. Mater. Chem. B*, 2023, **11**(2), 415–429.

40 L. Chen, G. Chen, K. Hu, L. Chen, Z. Zeng, B. Li, G. Jiang and Y. Liu, Combined photothermal and photodynamic therapy enhances ferroptosis to prevent cancer recurrence after surgery using nanoparticle-hydrogel composite, *Chem. Eng. J.*, 2023, **468**, 143685.

41 R. Arshad, T. H. Bokhari, T. Javed, I. A. Bhatti, S. Rasheed, M. Iqbal, A. Nazir, S. Naz, M. I. Khan, M. K. Khosa and M. Zia-ur-Rehman, Degradation product distribution of Reactive Red-147 dye treated by $UV/H_2O_2/TiO2$ advanced oxidation process, *J. Mater. Res. Technol.*, 2020, **9**(3), 3168–3178.

42 H. He, L. Du, M. Tan, Y. Chen, L. Lu, Y. An, Y. Wang, X. Li, B. Li, J. Shen and J. Wu, Cleavable bimetallic-organic polymers for ROS mediated cascaded cancer therapy under the guidance of MRI through tumor hypoxia relief strategy, *Sci. China: Chem.*, 2020, **63**, 936–945.

43 S. Baseeruddin Alvi, R. P S, N. Begum, A. B. Jogdand, B. Veeresh and A. K. Rengan, In situ nanotransformable hydrogel for chemo-photothermal therapy of localized tumors and targeted therapy of highly metastatic tumors, *ACS Appl. Mater. Interfaces*, 2021, **13**(47), 55862–55878.

44 M. F. Attia, N. Anton, J. Wallyn, Z. Omran and T. F. Vandamme, An overview of active and passive targeting strategies to improve the nanocarriers efficiency to tumour sites, *J. Pharm. Pharmacol.*, 2019, **71**(8), 1185–1198.

45 H. Maeda and M. Khatami, Analyses of repeated failures in cancer therapy for solid tumors: poor tumor-selective drug delivery, low therapeutic efficacy and unsustainable costs, *Clin. Transl. Med.*, 2018, **7**, 1–20.

46 M. Yu and J. Zheng, Clearance pathways and tumor targeting of imaging nanoparticles, *ACS Nano*, 2015, **9**(7), 6655–6674.

47 R. Laurano and M. Boffito, Thermosensitive micellar hydrogels as vehicles to deliver drugs with different wettability, *Front. Bioeng. Biotechnol.*, 2020, **8**, 708.

48 M. Boffito, P. Sirianni, A. M. Di Rienzo and V. Chiono, Thermosensitive block copolymer hydrogels based on poly(ε–caprolactone) and polyethylene glycol for biomedical applications: state of the art and future perspectives, *J. Biomed. Mater. Res., Part A*, 2015, **103**(3), 1276–1290.

49 K. Kuperkar, S. Tiwari and P. Bahadur, Self-assembled block copolymer nanoaggregates for drug delivery applications, *Appl. Polym. Drug Delivery*, 2021, 423–447.